Quasi-10-day wave activity in the southern high-latitude MLT region and its relation to the large-scale instability and gravity wave drag

Wonseok Lee[1], In-Sun Song[1], Byeong-Gwon Song[1], Yong Ha Kim[2]

[1]Department of Atmospheric Sciences, Yonsei University, Seoul 03722, South Korea

[2]Department of Astronomy and Space Science, Chungnam National University, Daejeon 34134, South Korea

Correspondence to: In-Sun Song (songi@yonsei.ac.kr)

Abstract. Seasonal variation of westward-propagating quasi-10-day wave (Q10DW) in the mesosphere and lower thermosphere of the Southern Hemisphere (SH) high-latitude regions is investigated using meteor radar (MR) observations for the period of 2012–2016 and Specified Dynamics (SD) version of the Whole Atmosphere Community Climate Model (WACCM). The phase difference of meridional winds measured by two MRs located in Antarctica gives observational estimates of the amplitude and phase of Q10DW with zonal wavenumber 1 (W1). The amplitude of the observed Q10DW-W1 is large around equinoxes. In order to elucidate the variations of the observed Q10DW-W1 and its possible amplification mechanism, we carry out two SD-WACCM experiments nudged towards the MERRA-2 reanalysis from the surface up to ~60 km (EXP60) and ~75 km (EXP75). Results of the EXP75 indicate that the observed Q10DW-W1 can be amplified around the barotropic/baroclinic instability regions in the middle mesosphere around 60°S–70°S. In the EXP60, it is also found that Q10DW-W1 is amplified around the instability regions, but the amplitude is too large compared with MR observations. The large-scale instability in the EXP60 in the SH summer mesosphere is stronger than that in the EXP75 and Microwave Limb Sounder observation. The larger instability in the EXP60 is related to the large meridional and vertical variations of polar mesospheric zonal winds in association with gravity wave parameterization (GWP). Given uncertainties inherent in GWP, these results can suggest that it is possible for models to spuriously generate traveling planetary waves such as Q10DW, especially in summer, due to the excessively strong large-scale instability in the SH high-latitude mesosphere.

1. Introduction

A series of Rossby normal modes (free oscillations) is the homogeneous solution of the governing equations on a sphere linearized with respect to the isothermal and quiescent reference atmosphere (e.g., Andrews et al., 1987; Forbes et al., 1995; Salby, 1984). Traveling normal modes exhibit clear planetary-scale spatiotemporal oscillations throughout the whole atmosphere, and for sufficiently large amplitudes, these traveling planetary waves (PWs) can play an important role in the momentum and energy transfer to the mean flow (Salby, 1984). Three gravest traveling normal modes have been observed: Westward-propagating zonal-wavenumber-1 PWs with periods of approximately 5, 10, and 16 days. The classical wave theory based on the isothermal and quiescent atmosphere gives the theoretical periods of 5, 8.3, and 12.5 day, but the periods in the real atmosphere can be shifted to values close to 5, 10, and 16 days, respectively (Salby, 1981a, b), due to influences of the vertical and meridional variation of the mean horizontal winds and temperature.

Among the gravest modes, the quasi-5-day wave (Q5DW) and quasi-16-day wave (Q16DW) have extensively been studied through observations, modeling, and assimilation products: Ground-based observations (e.g., Day and Mitchell, 2010; He et al., 2020b; Mitra et al., 2022), satellite observations (e.g., Forbes and Zhang, 2017; Huang et al., 2022), reanalysis data (e.g., Huang et al., 2017), and simulations (e.g., Qin et al., 2021). Using meteor radars (MRs) located in the northern and southern polar regions, Day and Mitchell (2010) showed that PW activity is strong during winter and the seasonal variation of PW is similar in both polar regions. According to Qin et al. (2021) and Mitra et al. (2022), the barotropic and baroclinic instabilities are the possible

57 sources of Q5DW and Q16DW in that the waves can draw energy from the mean flow

58 in the instability region. The disturbance of zonal-mean flow frequently occurs during

59 the large-scale meteorological events such as sudden stratospheric warming (SSW). It

60 has been reported that the amplitude of Q5DW or Q16DW increases during SSW events

61 (Eswaraiah et al., 2016; Lee et al., 2021; Li et al., 2021; Ma et al., 2022). In addition,

62 the amplified PWs can interact with tidal waves through the in-situ nonlinear

63 interaction, resulting ionospheric disturbances during SSW (e.g., Goncharenko et al.,

64 2020; Forbes et al., 2021; Liu et al., 2021; Qin et al., 2019).

65   In contrast, the westward propagating quasi-10-day wave (Q10DW) with zonal

66 wavenumber 1 (W1) has received little attention compared to the other gravest normal

67 modes. Forbes and Zhang (2015) showed that Q10DW-W1 has a mean period of 9.8 ±

68 0.4 days using the temperature measurements from the Sounding of the Atmosphere

69 using Broadband Emission Radiometry (SABER) instrument mounted on NASA's

70 TIMED (Thermosphere Ionosphere Mesosphere Energetics Dynamics) satellite in

71 2002–2013. They presented that the large amplitude of Q10DW-W1 is found in the

72 mid-latitude (40–50° latitude) mesosphere and lower thermosphere (MLT) region of

73 both hemispheres in equinoxes, although their results are limited to the latitude of 50°

74 because of the yaw cycle of the satellite. Hirooka (2000) reported that the global

75 structure of Q10DW-W1 using the Improved Stratosphere and Mesospheric Souder

76 (ISAMS) instrument aboard Upper Atmosphere Research Satellite (UARS) from

77 November 1991 to May 1992. The results also showed that the Q10DW-W1 is active

78 during equinoxes and winter at 0.1 hPa (~65 km). In addition, it is found that

79 nonuniform and background zonal wind field can influence the structure of the wave in

80 the mesosphere. The amplitude of the Q10DW-W1 is uniform or decays in the vertical

81 near the mesopause, and it does not increase above the mesosphere, even though the

82 critical layer is absent. Using the airglow intensities simulated by the global circulation

83 model assimilated by the reanalysis data from ground to 30 km, Egito et al. (2017) also

84 found that the 10-day oscillation is dominant from autumn to spring in the mid-latitude

85 MLT region. More recently, Huang et al. (2021) investigated the Q10DW activity based

86 on the Modern-Era Retrospective analysis for Research and Applications version 2

87 (MERRA-2) reanalysis data. They showed that the dominant components of Q10DW

88 are westward-propagating waves with zonal wavenumber 1 during winter and spring in

89 the stratosphere and mesosphere and eastward-propagating waves with zonal

90 wavenumber 1 and 2, which are excited in the mesospheric instability region. Although

91 both westward and eastward Q10DW modes are found, they mainly focus on the

92 eastward propagating Q10DW.

93   Several studies have investigated the response of Q10DW-W1 to SSWs.

94 Matthias et al. (2012) conducted a composite analysis of wave activities during major

95 Northern Hemisphere (NH) SSWs from 1989 to 1998, revealing an amplification of

96 Q10DW-W1 in the NH high-latitude MLT region following major SSW events. He et

97 al. (2022a2020a, 2022b2020b) utilized NH MRs to observe the occurrence of Q10DW-

98 W1 and Q16DW-W1 during four winter major SSWs. They found that these waves

99 persisted for approximately three to five whole cycles during the events. Chandran et al.

100 (2013) examined the forcing of secondary PWs-W1 driven by stratospheric instability

101 on zonal winds as a response to 2012 NH minor SSW. Sassi and Liu (2014) conducted

102 numerical simulations during minor and major NH SSWs and solar minimum condition.

103 They found that PWs-W1 with periods between 2 and 10 days originating in the high-

104 latitude NH could propagate equatorward and influence equatorially trapped tides. This

105 equatorward propagation of secondary PWs was also reported by Qin et al. (2022).

106 They suggested that secondary PWs-W1 with periods of 10 to 16 days generated in the

107 high-latitude NH during sudden stratospheric final warming could impact the Southern

108 Hemisphere (SH) stratosphere, depending on the phase of Quasi-Biennial Oscillation

109 (QBO). In the SH, studies by Lee et al. (2021) and Wang et al. (2021) using SH MRs

110 reported that Q10DW was amplified prior to 2019 SH SSW. Yamazaki and Matthias

111 (2019) reported that the Q10DW-W1 is not only intensified during SSWs but also

112 affected by seasonal timing of SSWs (i.e., final stratospheric warming) in stratospheric

113 instability regions.

114   While the amplification mechanism of Q10DW-W1 generated following SSWs

115 has been addressed in previous studies (e.g., Qin et al., 2022, Yin et al., 2023), the

116 specific mechanisms driving their seasonal amplification during equinoxes remain less

117 explored. In the present study, we focus on the seasonal variation of Q10DW-W1 in the

118 SH high-latitude MLT region using MRs located in Antarctica. Plus, we carry out

119 numerical simulations using the Specified Dynamics version of the Whole Atmosphere

120 Community Climate Model (SD-WACCM) nudged towards MERRA-2 reanalysis data

121 in order to elucidate the observed Q10DW-W1 and its amplification mechanism.

122 Section 2 describes two MRs located in the Davis station (68.6°S, 77.9°E) and King

123 Sejong Station (KSS; 62.2°S, 58.8°W) and how we obtain Q10DW-W1 from the

124 observations. Also, the SD-WACCM experiments and Microwave Limb Sounder

125 (MLS) data used for validation are described in Section 2. Results are presented in

126 Section 3. In Section 3.1, we show seasonal variation of observed and modeled

127 Q10DW-W1 in the SH high-latitude MLT region. The amplification mechanism of

128 Q10DW is discussed in Section 3.2. Q10DW activities from SD-WACCM simulations

129 are demonstrated in Section 3.3. In Section 4, the results are summarized, and their

130 implications are discussed.

131

2. Data and Method

2.1 Meteor Radars

134   In this study, we use two MRs located in the Davis station (68.6°S, 77.9°E) and

135 King Sejong Station (KSS; 62.2°S, 58.8°W), Antarctica from 2012 to 2016. The

136 operating frequencies of both Davis and KSS MRs are 33.2 MHz and the peak powers

137 are 6.8 kW and 12 kW, respectively. Details of the operation parameters of Davis and

138 KSS are summarized in Holdsworth et al. (2008) and Lee et al. (2018), respectively. A

139 large number of studies has been performed to investigate the PW or tidal activities in

140 the MLT region with a single-station measurements of horizontal winds from an MR

141 (e.g., Eswaraiah et al., 2019; Luo et al., 2021; Wang et al., 2021; Liu et al., 2022; Lee et

142 al., 2021). However, single-station analysis has a limitation in diagnosing the wave

143 propagation direction, and thus most of such studies focused on the timing of

144 occurrence and amplitude variations of wave with a particular periodicity. For detailed

145 analysis of PWs based on the Rossby normal modes, propagation directions and

146 wavenumbers need to be considered. Recently, He et al. (2018) developed a method of

147 estimating wave propagation direction and wavenumber as well as amplitude by

148 adopting Phase Differencing Technique (PDT) to longitudinally separated MR

149 observations based on the method of Walker et al. (2004). Since the longitude

150 difference (λ_Δ) between Davis and KSS is about 137°, it is appropriate for analyzing

151 PWs with zonal wavenumber 1 by applying the PDT. In order to estimate the zonal

152 wavenumber (s), we first make a continuous wavelet transform from the daily-mean

153 Davis and KSS MRs data ($W_{(f,t)}^{Davis}, W_{(f,t)}^{KSS}$), respectively, using the Morlet wavelet

154 function as a mother wavelet function (Torrence and Compo, 1998). Then, the cross

155 wavelet spectrum $C_{(f,t)}$ is derived: $C_{(f,t)} = W_{(f,t)}^{*Davis} W_{(f,t)}^{KSS}$, where * denotes the complex

156 conjugate. Using the phase difference (θ_Δ) obtained from $\theta_\Delta = \text{Arg}(C_{(f,t)})$ at a given

157 frequency and time, we estimate zonal wavenumber (s): $s = (-\theta_\Delta/(2\pi) + C)/\lambda_\Delta$. In

158 this study, we focus on the PW activity with $s = 1$, and the number of whole wave cycle

159 (C) between two stations is set to be zero (see He et al., 2018 for detailed PDT analysis).

160   Classical wave theory shows that the latitudinal structures of zonal and

161 meridional wind components for Q10DW normal mode from the Laplace tidal equation

162 are antisymmetric and symmetric with respect to the equator, respectively (e.g., Figure 1

163 in Yamazaki and Matthias, 2019). The magnitude of Q10DW-W1 has maxima at the

164 latitude of 25° and poles for zonal and meridional wind components, respectively.

165 Around the latitude of 65°S close to the latitudes of the two MR observation sites, the

166 normalized amplitude of Q10DW-W1 normal mode for the zonal wind is nearly zero,

167 but the normalized normal mode magnitude for the meridional wind is larger than the

168 half of the maximum magnitude for the meridional wind (Yamazaki and Matthias,

169 2019). For this reason, daily-mean meridional wind data from the MRs is used for the

170 Q10DW analysis.

171

172 **2.2 SD-WACCM**

173   In this study, for detailed analysis of the observed Q10DW-W1 activity and its

174 amplification mechanism, we compare observational results with Q10DW-W1

175   simulated using the Specified Dynamics (SD) version of WACCM version 4 (Marsh et

176   al., 2013). WACCM4 is a high-top (up to the lower thermosphere about 140 km)

177   atmospheric component model of the Community Earth System Model developed at the

178   National Center for Atmospheric Research. WACCM4 employs Community

179   Atmospheric Model (CAM) version 4 physics package. The default horizontal

180   resolution of WACCM4 is $1.9° \times 2.5°$ (lat. $\times$ long.), and it uses the 88 hybrid sigma

181   vertical levels for the SD mode. Since we focus on the PWs such as Q10DW-W1, daily-

182   mean values from the SD-WACCM are used. In this study, two SD-WACCM

183   experiments with two different nudging depths (EXP60 and EXP75) are performed. In

184   the EXP60 and EXP75, model variables are nudged towards the MERRA-2 reanalysis

185   data from surface to about 60 km in altitude and 75 km, respectively. The MERRA-2

186   reanalysis is produced by assimilating various types of observations into the Goddard

187   Earth Observing System version 6 (GEOS-6) global model (Gelaro et al., 2017). In

188   addition to conventional meteorological observations and operational satellite

189   measurements, the Earth Observing System (EOS) Aura MLS temperature and ozone

190   data are included in the assimilation procedure of the MERRA-2 from 5 hPa (~37 km)

191   up to 0.02 hPa (~75 km) and from 250 hPa (~10 km) to 0.1 hPa (~65 km), respectively

192   (Gelaro et al., 2017; McCormack et al., 2021). There is a divergence damping layer near

193   the top boundary of the GEOS-6 model used for production of the MERRA-2 reanalysis

194   (Fujiwara et al., 2017). The divergence damping is often used to effectively and

195   selectively remove high-frequency (noisy) gravity waves keeping the large-scale

196   circulation and PWs structure less changed (Jablonowski and Williamson, 2011). As a

197   result, MERRA-2 reanalysis can reflect the large-scale MLT variabilities (e.g.,

198   McCormack et al., 2021; Harvey et al., 2021). As suggested by Brakebusch et al.

199 (2013), nudging coefficients for EXP60 and EXP75 are 0.01 s^{-1} below the altitudes of

200 50 km and 65 km, respectively, and they linearly decrease and become zero above the

201 altitudes of 60 km and 75 km, respectively.

202   WACCM simulation requires the data of sea surface temperature, sea ice

203 fraction, solar and geomagnetic indices, and ionization rate by energetic particle

204 precipitation (EPP) for the time period of simulations. The sea surface temperature and

205 sea ice fraction data are produced by the NOAA Optimum Interpolation (Reynolds et

206 al., 2002). The solar and geomagnetic indices are obtained from NASA GSFC/SPDF

207 OMNIWeb interface (https://omniweb.gsfc.nasa.gov/ow.html). The EPP ionization rate

208 is provided by the CCMI reference-C2 data for the period of 1960–2100 (Eyring et al.,

209 2013). Regarding MLT dynamics, effects of gravity wave drag (GWD) are crucial.

210 WACCM includes a suite of GWD parameterizations (Richter et al., 2010) for effects of

211 unresolved GW momentum transfer from orography (McFarlane, 1987), deep

212 convection (Beres et al., 2005), and frontal activity (Charron and Manzini, 2002). SD-

213 WACCM simulations start from January 1, 2011 and end at the end of 2016. First one-

214 year results are discarded as a spin-up, and results for 2012–2016 are compared with

215 MR observations.

216

217 **2.3 MLS**

218   For validation of Q10DW-W1 estimates obtained from MR observations, we

219 derive the geostrophic winds from geopotential height (GPH) data (version 5.1 product)

220 measured using MLS onboard the NASA's EOS Aura satellite (Schwartz et al., 2008).

221 Geostrophic wind components are computed following Matthias and Ern (2018). The

222 Aura satellite launched on July 2004 is in a sun-synchronous orbit with an altitude of

223 705 km. Spatial coverage of MLS instrument is from 82°S to 82°N with a 165 km

224 resolution along the track. The sun-synchronous orbit of Aura satellite can provide a

225 global coverage data per day with about 15 orbits. The global coverage of GPH is

226 produced using daily mean values in 5°×5° (lat. × long.) grids. In this process, GPH

227 data is filtered on the basis of the recommended precision, status, quality, and

228 convergence thresholds of Version 5.0 Level 2 and 3 data quality and description

229 document (https://mls.jpl.nasa.gov/data/v5-0_data_quality_document.pdf).

230

231 **3. Results and Discussion**

232 **3.1 Seasonal variation of Q10DW-W1 in the MLT region**

233   The perturbation meridional wind for Q10DW-W1 is symmetric in latitude

234 about the equator as mentioned earlier. Therefore, in order to extract and analyze

235 Q10DW-W1, which is potentially related to the Rossby normal mode in the MLT

236 region, it is necessary to confirm whether the latitudinal structure of Q10DW-W1 has

237 the hemispheric symmetry. Although the KSS and Davis MR observations can provide

238 information about the longitudinal propagation of Q10DW-W1, it is impossible to

239 estimate the latitudinal structure using these radars alone. In this study, the meridional

240 geostrophic winds obtained from the MLS geopotential data are used to confirm the

241 hemispheric symmetry of Q10DW-W1 estimated from MRs. The amplitudes of

242 Q10DW-W1 in the MLS are obtained using the two-dimensional Fast Fourier transform

243 (FFT) of the geostrophic meridional winds averaged over the height range of 80–90 km

244 in time (30-day sliding window) and longitude domain. The time-latitude cross section

245 of the amplitude of Q10DW-W1 derived from the MLS geostrophic meridional wind

246 averaged over the height range of 80–90 km is presented in the Supplement (Fig. S1).

247 Hereafter, the Q10DW denotes westward-propagating quasi-10-day normal mode wave

248 with zonal wavenumber 1 and the hemispheric symmetry, where quasi-10-day

249 periodicity means the periods between 9 and 11 days. Unless the hemispheric symmetry

250 is satisfied, the analyzed westward propagating signals with zonal wavenumber 1 are

251 referred to as quasi-10-day-like oscillations (Q10DOs).

252   Figure 1 shows the time-height distributions of the amplitudes of Q10DWs and

253 Q10DOs derived from the daily-mean meridional winds observed at the Davis and KSS

254 MRs using the PDT method. The regions shaded in gray represent the time periods

255 when the hemispheric symmetry is not found in the MLS results as shown in Fig. S1.

256 The time periods of the hemispheric symmetries are defined by the periods when the

257 amplitudes of the MLS meridional geostrophic winds (vertically averaged over 80–90

258 km) with quasi-10-day periodicity exceed 3.5 m s^{-1} in both 60°N–80°N and 60°S–80°S.

259 The MLS results in solstices are generally shaded in gray (see Fig. S1). This result

260 indicates that Q10DWs in a form of normal modes are found during equinoxes, which is

261 consistent with the results from Forbes and Zhang (2015). Using the periods of the

262 hemispheric symmetry of the Q10DW obtained from the MLS, we identify the normal

263 mode Q10DW from the Davis and KSS MR observations.

264   The 5-yr average (The bottom-most panel of Fig. 1) between 2012 and 2016

265 indicates that the Q10DWs are generally enhanced from late February to April and from

266 late August to September in the altitude range of 82–98 km with the maximum

267 amplitude of 2.6 m s^{-1}. The Q10DWs are usually more amplified in early spring from

268 late August to September with the largest amplitudes around the altitudes of 90–95 km.

269 Large amplitudes are found in winter (July to mid-August), but they are unlikely to

270 represent the normal mode Q10DWs, as it is clear from the gray shading in winter.

271 According to Wang et al. (2021), the nonlinear wave-wave interaction can generate

272 Q10DOs in southern winter. Their Q10DOs are eastward propagating, interacting with

273 stationary PWs with zonal wavenumber 1. Meanwhile, the Q10DWs and Q10DOs (Fig.

274 1) obtained from two MRs using the PDT method are westward propagating.

275 Understanding of the mechanisms of the winter-time westward-propagating Q10DOs is

276 beyond the scope of this study, and it requires continuing researches. It is important to

277 note that the amplitudes of Q10DW are systematically lower in MRs compared to the

278 MLS results. These discrepancies might be attributed to the accuracy of estimated

279 geostrophic winds from the MLS data, or the inherent limitations of MR analysis, which

280 in our case involves only two stations located at slightly different latitudes.

281   For individual years, it is also found that the amplitude of Q10DW is generally

282 large in equinoxes (see panels for each year in Figs. 1 and S1). During March–April

283 (autumn), active Q10DWs are identified, and their amplitudes reach up to ~3 m s^{-1} in

284 2014 and 2015. Particularly, the peak in September (spring) is prominent in 2016. These

285 MR observation results are remarkably consistent with results obtained using satellite

286 geopotential height in the SH high-latitude region (Forbes and Zhang, 2015).

287 Occasionally, large amplitude Q10DWs are observed near the altitude of 98–100 km in

288 equinoxes (e.g., April 2015), but results around 100 km can be less reliable because the

289 number of MR echoes above 96 km is much smaller than that around 90 km (Lee et al.,
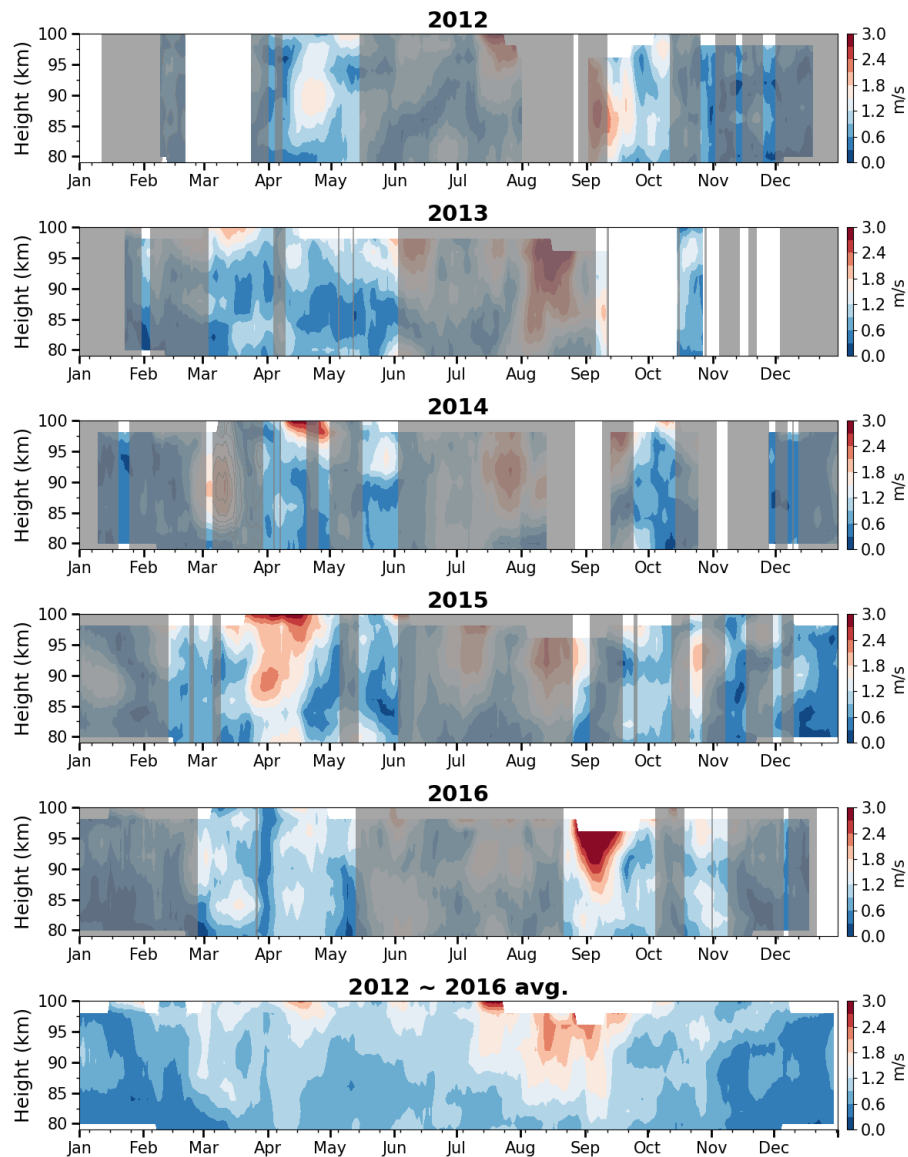
290 2022).

Figure 1. Time-height distributions of the amplitudes of Q10DWs (unshaded region) and Q10DOs (shaded region) derived from meridional winds observed by MRs at Davis (68.6°S, 77.9°E) and KSS (62.2°S, 58.8°W) for 2012–2016. The bottom-most panel shows the 5-yr average from 2012 to 2016. The gray shading represents time periods where the hemispheric symmetry is unclear in the MLS results (see the text for details of the unclearness of symmetry).

298   Figure 2 demonstrates the time-height distributions of the amplitudes of

299   Q10DWs and Q10DOs around the latitude of 63°S in the EXP75 SD-WACCM

300   simulation for the altitude range of 60–110 km for 2012–2016, along with the

301   hemispheric symmetry period obtained from the MLS results. The bottom-most panel of

302   Fig. 2 shows the 5-yr average from 2012 to 2016. The amplitudes are obtained by

303   decomposing the meridional winds obtained from the simulation into westward

304   propagating Fourier modes with zonal wavenumber 1 using the 2D FFT in time (30-day

305   sliding window) and longitude domain around 63°S. From Fig. 2, it is clear that the

306   seasonal variations of Q10DW amplitudes obtained from the simulation have year-to-

307   year variations, as in the Q10DW amplitudes derived from the two MRs. However, the

308   Q10DW activities observed from the MR observations are ~~generally larger~~much smaller

309   than those in the EXP75 simulation (see Fig. 1).

310   The 5-yr average in Fig. 2 shows that there are four main time periods

311   (February, April, September, November) when the modeled Q10DWs and Q10DOs are

312   active in the EXP75. The time periods of April and September are consistent with the

313   MR observations in terms of Q10DW amplitudes and the hemispheric symmetry

314   obtained from the MLS, but the other periods are not. The active signals simulated in

315   February and November do not appear to be normal mode Q10DWs because the

316   hemispheric symmetry is not seen in the MLS data during February and November. For

317   a more comprehensive understanding of the Q10DOs in the EXP75 during February and

318   November, we will discuss in more detail later in Section 3.3 by comparing between the

319   EXP75 and EXP60.

320
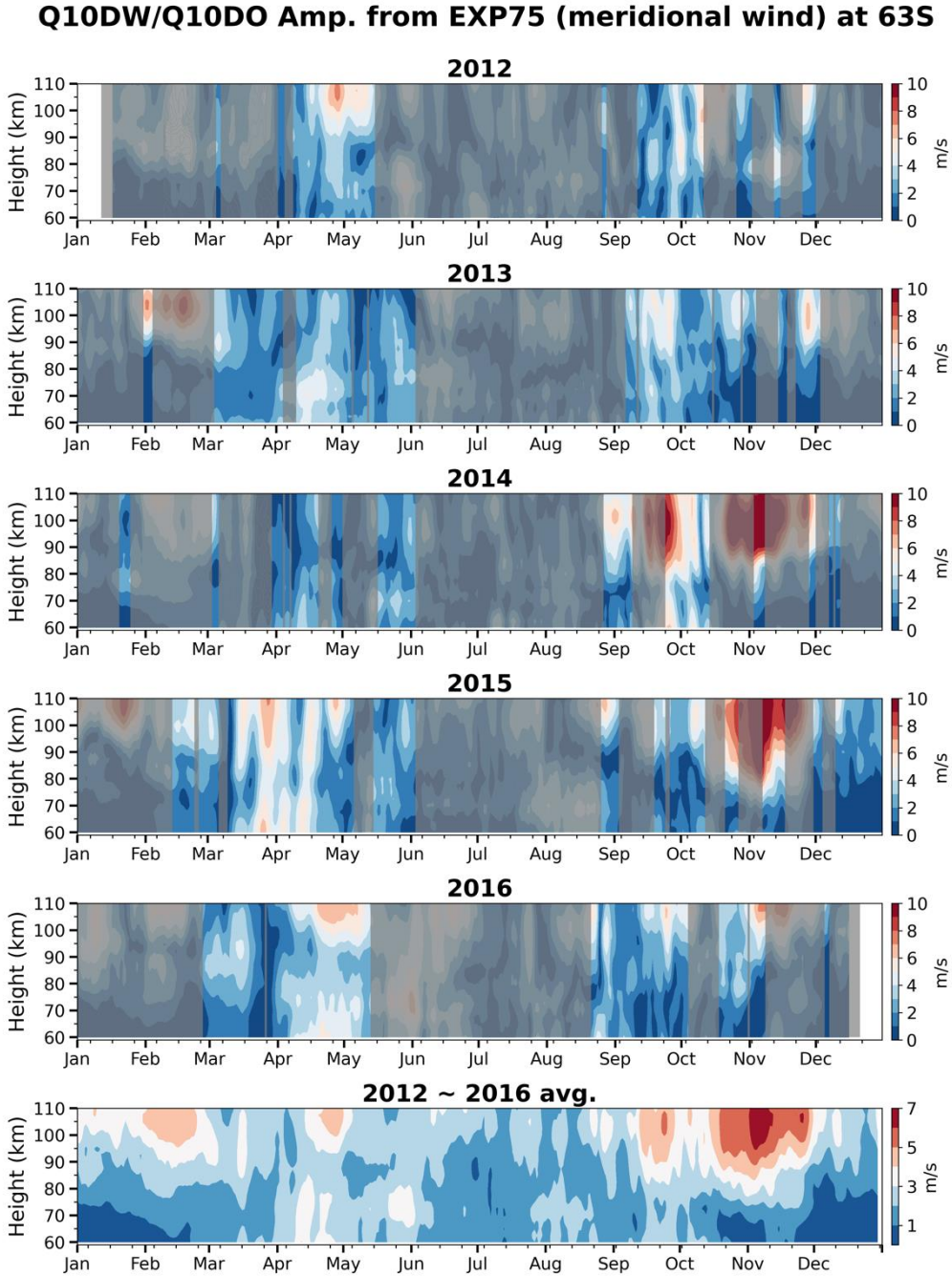
Figure 2. Time-height distributions of the amplitudes of Q10DWs (unshaded region) and Q10DOs (shaded region) around 63°S for 2012–2016 in the EXP75. The bottom-most panel shows the 5-yr average between 2012 and 2016. The gray shaded areas represent periods where the hemispheric symmetry is not observed in the MLS results.

325   Figure 3 shows time series of the normalized amplitudes of Q10DWs and

326   Q10DOs obtained from the MR observations (black) and EXP75 simulation (blue).

327   Normalization is carried out by averaging the amplitudes in the altitude range between

328   80 and 100 km and dividing the 5-yr averaged values by the respective maximum

329   values in the same altitude range. We select the dates when (i) the amplitudes obtained

330   from both MRs and EXP75 exceed their respective 5-yr mean values, (ii) their

331   correlation is relatively large (> 0.6), and (iii) the hemispheric symmetry occurs in the

332   MLS results. The correlation coefficients are computed for sliding 7-day windows with

333   1-day step. The dates when the three criteria are satisfied are represented by yellow

334   boxes on abscissa in Fig. 3. The total number of the dates when the Q10DW was

335   substantially active in both observations and model (EXP75) is 46. Using EXP75 results

336   on the selected dates, the amplification mechanisms of the observed Q10DW will be

337   discussed.
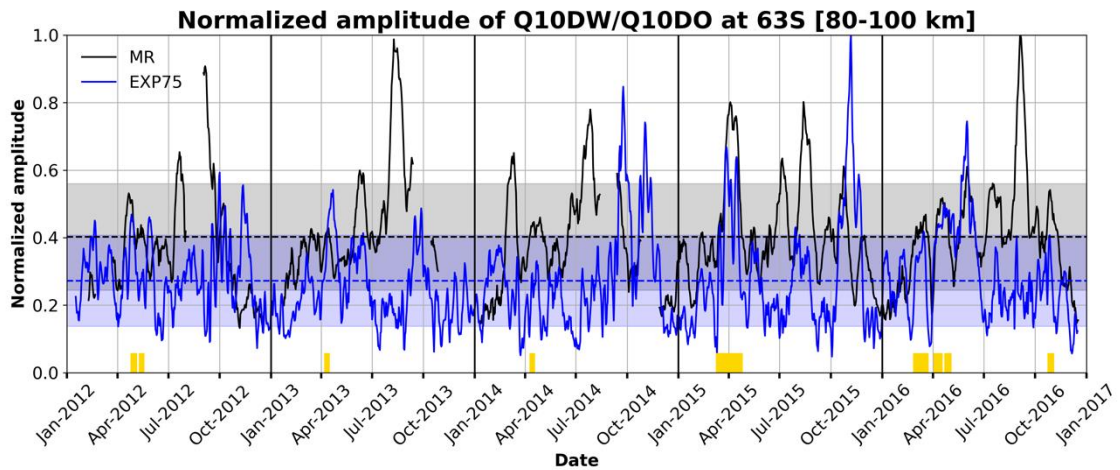
338

339 **Figure 3.** Time series of normalized amplitudes of Q10DW/Q10DOs from the

340 observations (black line) and EXP75 simulation (blue line). The dashed lines and

341 shaded areas represent the mean and standard deviation of normalized amplitude of

342 Q10DW/Q10DOs from the observations (black) and EXP75 (blue), respectively.

343 Yellow boxes on abscissa indicate the dates when the normalized amplitudes from both

344 MRs and EXP75 can be considered to be due to the normal mode Q10DWs.

3.2 Amplification mechanisms of Q10DW

The amplitude of upward propagating PWs grows with height when their vertical propagation is allowed, but it can decrease with height in the evanescent region where the square of refractive index n^2 becomes negative. Regions of negative n^2 are often accompanied by regions of the negative latitudinal gradient of zonal-mean potential vorticity ($\bar{q}_\phi$), where $\bar{q}$ is the zonal-mean quasi-geostrophic potential vorticity (QGPV), the overbar denotes zonal averaging, ϕ is the latitude, and the subscript ϕ denotes the partial derivative in the latitudinal direction. In the regions of negative $\bar{q}_\phi$, the barotropic and baroclinic instabilities can occur (Matsuno, 1970), and it is known that PWs can amplify extracting energy from the mean flow while they pass through the instability regions (Meyer and Forbes, 1997; Cohen et al., 2013). If PWs somehow reach their critical lines within an instability region, it is possible for these PWs to tunnel through the critical lines (Rhodes et al., 2021). In case that the evanescent region is thin enough, and the PWs can reach their critical lines, it is also possible for the overreflection to take place, resulting in the amplified PWs and the propagation of the amplified PWs out of the overreflection region (Lindzen et al., 1980; Rhodes et al., 2021).

Another possible way of modulating PWs is their excitation by the nonconservative GW forcing (Song et al., 2020). Nonconservative GWD forcing (NCGWD; Z') can generate PWs as it is clearly seen from the perturbation QGPV equation given in the form of wave action conservation equation (1) when diabatic forcing is ignored in Z' [see Andrews et al. (1987) and Palmer (1982) for details]:

368 $\quad \frac{\partial A}{\partial t} + \boldsymbol{\nabla} \cdot \mathbf{F} = \rho_0 \overline{Z' q'_{(M)}} / (\bar{q}_\phi / a\textcolor{blue}{a}),$ $\hfill$ (1)

369

370 where a is the earth's mean radius; ρ_0 is the reference density given as an exponentially

371 decreasing function of log-pressure height z; the prime denotes the perturbation from the

372 respective zonal mean; A, defined below using $q'_{(M)}$, is the wave-activity density in the

373 spherical QG system; $q'_{(M)}$ is the perturbation of modified QGPV, modified to consider

374 the planetary vorticity advection by the isallobaric meridional wind in spherical geometry

375 (Matsuno, 1970; Palmer, 1982); Z' is the curl of the horizontal GWD perturbation; $\boldsymbol{\nabla} \cdot \mathbf{F}$

376 is the divergence of Eliassen-Palm (EP) flux ($\mathbf{F}$), and the flux $\mathbf{F}$ is considered to be the

377 wave-activity flux given by $\mathbf{F} = \mathbf{c}_g A$ in the QG framework, where $\mathbf{c}_g$ is the group velocity

378 in the latitude-height domain.

379 $\qquad$ In (1), the wave-activity density A and the modified QGPV perturbation $q'_{(M)}$ are

380 given in spherical geometry (Palmer, 1982), respectively, as follows:

381

382 $\quad A = a \cos \phi \, \frac{1}{2} \rho_0 \frac{\overline{q'^2_{(M)}}}{\bar{q}_\phi / a},$ $\hfill$ (2)

383 $\quad q'_{(M)} = \frac{v'_\lambda}{a \cos \phi} - \frac{f}{a \cos \phi} \left(\frac{u' \cos \phi}{f} \right)_\phi + \frac{f}{\rho_0} \left(\rho_0 \frac{\theta'}{\bar{\theta}_z} \right)_z,$ $\hfill$ (3)

384

385 where u and v are zonal and meridional wind components, respectively; λ is the

386 longitude; f is the Coriolis parameter; θ is the potential temperature. The subscript λ and

387 z mean the partial derivatives in longitude and vertical directions, respectively.

388   For understanding of amplification of PWs around the instability regions, the

389   barotropic and baroclinic instability regions are determined by the negative sign of $\bar{q}_\phi$

390   (Andrews et al. 1987) given by:

391

392   $\bar{q}_\phi = 2\Omega \cos\phi - \left[\frac{(\bar{u}\cos\phi)_\phi}{a\cos\phi}\right]_\phi - \frac{a}{\rho_0}\left(\frac{\rho_0 f^2}{N^2}\bar{u}_z\right)_z ,$ (4)

393

394   where Ω is the earth's rotation rate and N is the buoyancy frequency. The negative sign

395   of $\bar{q}_\phi$ is a necessary condition of the barotropic and baroclinic instabilities. The second

396   (with negative sign) and third (with negative sign) terms on the right-hand side of (4)

397   represent the meridional and vertical curvatures of the zonal-mean zonal wind,

398   respectively. If the second or third term is dominant, $\bar{q}_\phi$ can become negative, and the

399   instabilities can take place.

400   The square of refractive index n^2 is used to analyze the propagation

401   characteristics of PWs and depends on the mean QGPV gradient as follows:

402

403   $n^2 = \frac{\bar{q}_\phi}{a(\bar{u}-c)} - \frac{s^2}{a^2\cos^2\phi} - \frac{f^2}{4N^2H^2},$ (5)

404

405   where c is the zonal phase speed of single PW (i.e., $c = 2\pi a \cos\phi /(s\tau)$; s is the zonal

406   wavenumber, and τ is the wave period), and the constant scale height H is set equal to 7

407   km. The propagation of PWs is possible in regions of positive n^2. On the other hand,

408   PWs can be reflected or be evanescent in the region where $n^2 < 0$ (Matsuno, 1970).

409   In order to analyze the wave propagation and wave activity for the selected dates

410   for Q10DWs (or Q10DOs) found in MRs and model simulations, we use the EP flux as

411   diagnostic tools, derived in the Transformed Eulerian-Mean framework for the spherical

412   QG system (Palmer, 1982; Andrews et al., 1987). In the spherical geometry, the

413   meridional $[F^{(\phi)}]$ and vertical $[F^{(z)}]$ components of the EP flux $\mathbf{F} \equiv [0, F^{(\phi)}, F^{(z)}]$ are

414   given by

415

416   $F^{(\phi)} = -\rho_0 a \cos\phi \overline{u'v'}$,   (6)

417   $F^{(z)} = \rho_0 a \cos\phi f \overline{v'\theta'}/\bar{\theta}_z$,   (7)

418

419   Figure 4 shows the EP flux $\mathbf{F}$ and wave activity density normalized by $\rho_0 a\cos\phi$

420   for Q10DWs in the EXP75. The propagation inhibition region ($n^2 < 0$) and the

421   contours of zonal-mean zonal wind are overplotted. Thick green and black lines indicate

422   the regions of $\bar{q}_\phi = 0$ and of critical lines for Q10DWs, respectively. The critical lines

423   are plotted by computing the zonal phase speed (c) of Q10DW: $c = 2\pi a \cos\phi /(s\tau)$,

424   where $s = 1$ and $\tau = 10$ day. The wave-activity density is shaded in blue and red

425   depending on its sign [sgn(A)]. For the EP flux vector, $\mathbf{F}/\text{sgn}(A)$ ($= \mathbf{c}_g|A|$), rather than

426   $\mathbf{F}$ itself ($= \mathbf{c}_g A$), is plotted such that the EP flux can always be parallel to the local

427   group velocity of Q10DWs regardless of the instability regions where $\bar{q}_\phi < 0$ and thus

428   $A < 0$. For better illustration of the EP flux in the atmosphere where its density

429   decreases exponentially with height, the meridional and vertical components of EP flux

430   are scaled by $(p_s/p)^{0.85}[F^{(\phi)}/(a\pi), F^{(z)}/(3 \times 10^5)]$ (Edmon et al., 1980; Gan et al.,

431   2018), where p_s and p are the surface and atmospheric pressures, respectively.

432   For Fig. 4, we select the four dates of (a) 30 April 2012, (b) 11 April 2013, (c) 6

433   April 2015, and (d) 29 October 2016 when the three criteria mentioned in Fig. 3 are

434   satisfied (see yellow boxes in Fig. 3). That is, the normalized amplitudes of Q10DWs

435   from both MRs and EXP75 are larger than its average, the correlation coefficient is

436   larger than 0.6, and the hemispheric symmetry is found in the MLS results. The 30

437   April 2012 case (Fig. 4a) shows that the stratospheric jet is located around (40°S–60°S,

438   55 km) in the latitude-height domain and that there is a predominant branch of upward

439   and equatorward Q10DW EP flux vectors across the center of the stratospheric jet. In

440   the high-latitude mesosphere, there are two regions where both the large-scale

441   instability ($\bar{q}_\phi < 0$) and evanescence ($n^2 < 0$) take place, and they are located in

442   (55°S–65°S, 60–85 km) and (65°S–80°S, 70–110 km), respectively. Along the

443   instability boundaries (green lines), large positive or negative Q10DW activities are

444   found. Divergent EP flux vectors in the meridional direction are clearly seen around the

445   instability region located at (53°S, 65–75 km), which implies the excitation of Q10DWs

446   in association with the instability. In the region of MR observations (60°S–65°S, 85–

447   100 km), substantially amplified Q10DW activity appears, and the equatorward

448   Q10DW EP flux towards the MR sites is found over the amplified Q10DW activity.

449   Figure 4b demonstrates the case of 11 April 2013. One major branch of Q10DW

450   EP flux vectors (Fig. 4b) originates from the stratospheric jet located at (55°S–60°S,

451   45–60 km). In the southern and upper side of the stratospheric jet, the instability and

452   evanescent region extends from 45 km to 70 km height in the latitude of 50°S–75°S.

453 Above the instability region, distinct region of strong wave activity is found around

454 (50°S–65°S, 65–90 km), and this region is partially overlapped by the MR observation

455 region. Around this region, the Q10DW EP flux is directed downward and poleward

456 inside of the instability region (within green line). The Q10DW EP flux is directed

457 upward and equatorward outside and above the instability region. This diverging pattern

458 of EP flux around the instability region also shows the possibility of the excitation of

459 Q10DW in association with the instability.

460   For 6 April 2015 case (Fig. 4c), the structure of wave-activity density and

461 instability regions are similar to the 30 April 2012 case (Fig. 4a). The instability and

462 evanescent regions occur around (60°S–80°S, 70–100 km). Along the instability

463 boundaries, there are strong positive and negative wave-activity densities, and this

464 region of strong wave activities includes the MR observation region. Again, the

465 divergence of Q10DW fluxes appears in the upper part of the instability region around

466 (60°S–70°S, 80–100 km). The Q10DW propagates upward and equatorward outside of

467 the instability region and downward inside of the instability region, as in the other dates

468 shown in Figs. 4a and 4b. Unlike the other events, the propagation of Q10DW is

469 poleward in the stratosphere (30–60 km altitude). This result is consistent with Qin et al.

470 (2022). They reported that the meridional component of EP flux extends from the

471 stratosphere in the NH across the equator to the SH stratosphere during the westerly

472 phase of QBO in the middle stratosphere and during the westerly phase of the semi-

473 annual oscillation in the upper stratosphere.

474   In 29 October 2016 case (Figure 4d), the center of stratospheric jet is located

475 around (60°S–70°S, 20–30 km). Above the stratospheric jet, the eastward wind turns

476   westward around the altitude of 60 km. Within the region of westward wind, the

477   instability and evanescent regions are found. In addition, the critical lines exist inside

478   the instability region. The overreflection or transmission process can take place near the

479   critical lines as we mentioned. Notably, the significantly large positive and negative

480   wave-activity density regions are found around (45°S–70°S, 60–90 km) near the

481   instability boundaries, and these regions are partially overlapped by the MR observation

482   region. This result suggests that the observed amplification of Q10DW may be

483   attributed to the overreflection process. The EP flux of Q10DW predominantly

484   propagates upward and equatorward away from the strong wave-activity region around

485   (60°S, 60–70 km) with weak poleward propagation of Q10DW towards the instability

486   region across the critical lines.

487   For all the cases shown in Fig. 4, the results indicate that a distinct strong wave-

488   activity density region is located within the area observed by the MRs (around 60°S–

489   70°S and 80–100 km in height), associated with the large-scale instability region.

490   Considering the wave-activity density A is directly proportional and inverse

491   proportional to the $\overline{q'^2}$ and $\bar{q}_\phi$, respectively, it can be thought that the small $\bar{q}_\phi$

492   contributes the large magnitude of A near the instability region. However, we confirm

493   that the large $\overline{q'^2}$ is located around the instability region, leading to the overall large

494   wave-activity density (not shown in here). In addition, the group velocity of the wave is

495   given by $\mathbf{c}_g = \mathbf{F}/A$. For the selected cases (Fig. 4), the EP flux $\mathbf{F}$ in the MR observation

496   region is relatively small, while the magnitude of A is comparatively large. This

497   suggests a small group velocity in this region. These results agree with the study of

498 Thorncroft et al. (1993), which states that during the amplification of baroclinic waves,

499 the group velocity tends to be small.

500   As previously mentioned, Song et al. (2020) proposed that the NCGWD can

501 generate PWs. In addition, Forbes and Zhang (2015) suggested that the dissipation of

502 gravity waves filtered by the Q10DW wind field can generate a secondary Q10DW by

503 momentum deposition. In this regard, the both parameterized GWs and resolved GWs

504 ($s \geq 20$) could also play a role in generating Q10DW. To verify the contribution of

505 NCGWD, we analyze linearized disturbance QGPV equation (Andrews et al., 1987) for

506 the 4 cases shown in Fig. 4. Our analysis shows that the contribution of both NCGWD

507 and resolved GW for the Q10DW is negligible in the MLT region (see Fig. S3 in the

508 Supplement).

509   These results indicate that the large amplitudes of Q10DW observed in the SH

510 high-latitude region by the Davis and KSS MRs can originate from the high-latitude

511 stratosphere-mesosphere region, where the barotropic/baroclinic instability or

512 overreflection near the critical layer occur.

513
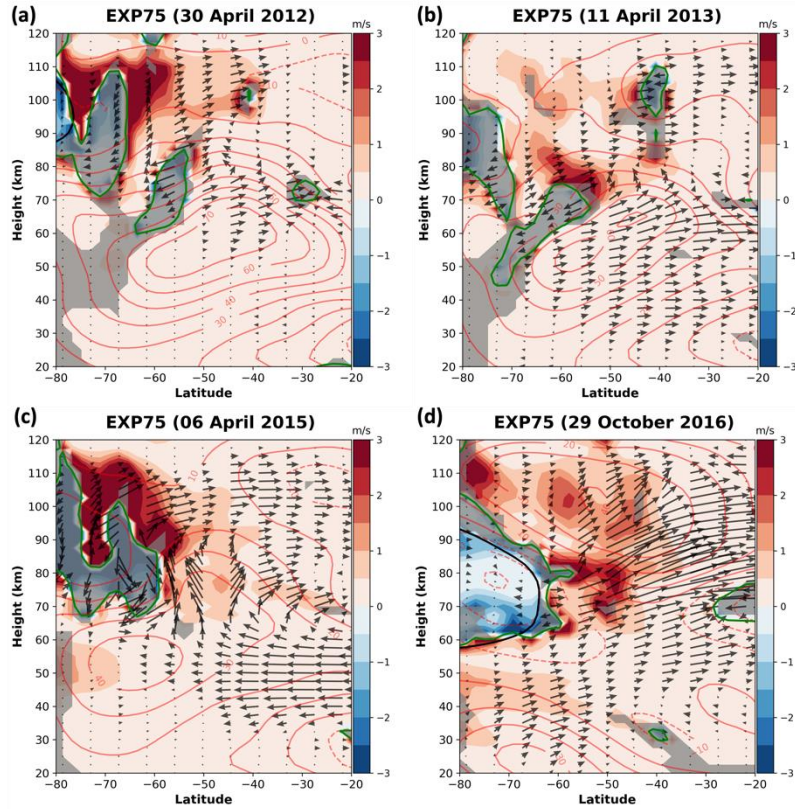
Figure 4. EP flux parallel to local group velocity [$\mathbf{F}/\mathrm{sgn}(A)$] and normalized wave

activity density [$A\,(\rho_0 a \cos\phi)^{-1}$ given in the unit of m s^{-1}] for the Q10DWs in the

EXP75 on (a) 30 April 2012, (b) 11 April 2013, (c) 6 April 2015, and (d) 29 October

2016. The activity density A is shaded in blue and red depending on its sign. The

boundaries of the instability regions ($\bar{q}_\phi = 0$, green lines), the negative n^2 regions (grey

shading), and the red contours for zonal-mean zonal wind are overplotted. For eastward

(westward) zonal-mean zonal wind, contours are plotted in solid (dashed) lines, and

contour interval is 10 m s^{-1}.

3.3 Comparison of Q10DO between SD-WACCM simulations

      This section compares the Q10DOs around the mesospheric instability regions

in the two SD-WACCM simulations (EXP75 and EXP60) for February and November.

525 February and November are chosen because the amplitudes of modeled Q10DOs are

526 substantial. The magnitude of Q10DO in the EXP75 is generally smaller than that in the

527 EXP60, which is more comparable to the MR and MLS observations in which both

528 Q10DWs and Q10DOs are weak (see Figs. S1 and S2 in the Supplement). Note that

529 more realistic meteorological fields are nudged throughout the mesosphere in the

530 EXP75. In this section, comparison between EXP75 and EXP60 for February and

531 November is carried out to reveal mechanisms behind weak Q10DOs in the EXP75.

532   Figure 5 demonstrates the properties of Q10DO and background atmospheric

533 conditions (as shown in Fig. 4) for 5 February 2013 and 16 November 2016 when the

534 Q10DO activity is found to be large in both simulations. The left and right panels of

535 Fig. 5 are the results from the EXP75 and EXP60, respectively. In Fig. 5, it is clear that

536 the strong wave-activity density for Q10DO arise in polar regions above the altitude of

537 70 km in the EXP60, and the magnitude of the EP fluxes in the EXP60 is much larger

538 than that in EXP75. In addition, in 5 February 2013 for the EXP60 (Fig. 5b), a

539 substantially strong wave-activity density region is located in the mid-latitude

540 mesospheric region as well. Around the strong wave-activity regions in the polar upper

541 mesosphere, it is seen that the EP fluxes of Q10DWs are divergent. In addition, the

542 distinct wave-activity density of Q10DO regions in the EXP60 occur along the

543 instability regions and critical lines around (50°S–70°S, 70–110 km) and (20°S–40°S,

544 65–80 km). On the other hand, the wave-activity density of Q10DO in the EXP75 (Fig.

545 5a and 5c) is located at relatively higher altitudes (80–100 km), and the strength of

546 Q10DO EP flux and wave-activity density are weaker than EXP60. Moreover, the

547 negative EP flux divergence (EPFD) is much larger in the EXP60 than in the EXP75

548 above the altitude of 80 km (not shown in here).

549   Our analysis reveals that the larger wave-activity density and EP fluxes in the

550   EXP60 along the large-scale instability region in the polar upper mesosphere compared

551   to the EXP75. This indicates that the stronger large-scale instability in the EXP60 can

552   amplify Q10DO activities, which is consistent with the analysis result that the

553   barotropic and baroclinic instabilities can be the major sources of the amplification of

554   traveling PWs (Harvey et al., 2019).
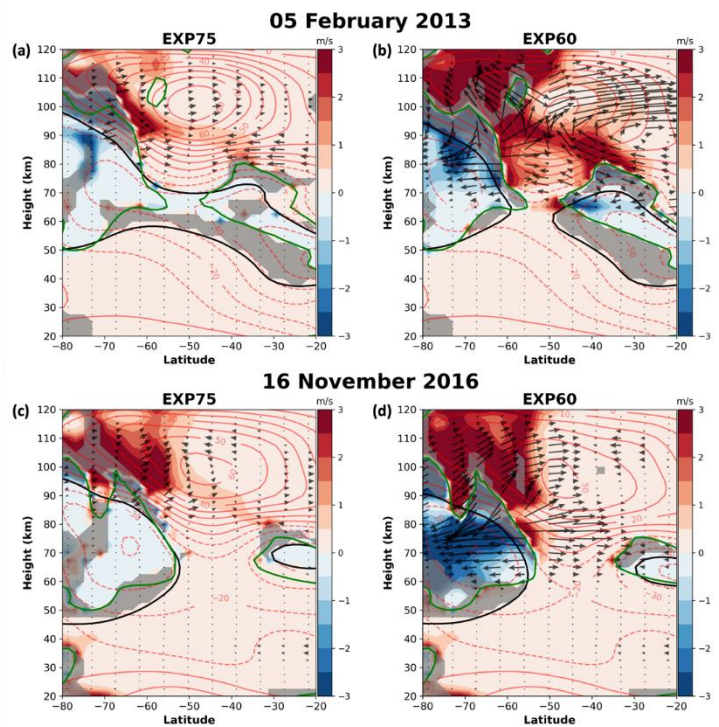
555

556 **Figure 5.** Same as Fig. 4 but for (a and b) 5 February 2013 and (c and d) 15 November

557 2016. The left and right columns represent the results from EXP75 and EXP60,

558 respectively.

559   Figure 6 shows the $\bar{q}_\phi$ (normalized by Ω) for 5 February 2013 and 16 November

560 2016 from the EXP75 (blue), EXP60 (red), and MLS (black). The normalization makes

561 $\bar{q}_\phi$ dimensionless. The $\bar{q}_\phi/\Omega$ from MLS is derived in the quasi-geostrophic framework

562   (Andrews et al., 1987) and it is included as a reference for validation. The $\bar{q}_\phi/\Omega$ is

563   averaged between the latitudes of 65°S-80°S where the wave-activity density is strong

564   and large negative $\bar{q}_\phi$ is found in Fig. 5. It is seen that the vertical profiles of $\bar{q}_\phi/\Omega$

565   from the EXP75 and MLS have somewhat small negative values and they are generally

566   similar below the altitude of 75 km, although the difference gradually increase above

567   the altitude of 75 km. On the other hand, large discrepancies are shown between EXP75

568   and EXP60 in the altitudes between 60–80 km. In the EXP60, $\bar{q}_\phi/\Omega$ has much larger

569   negative values, which suggest the relatively stronger barotropic or baroclinic instability

570   in the EXP60 and the amplification of the Q10DO in the mid-to-upper mesosphere in

571   association with the stronger instability in the EXP60.
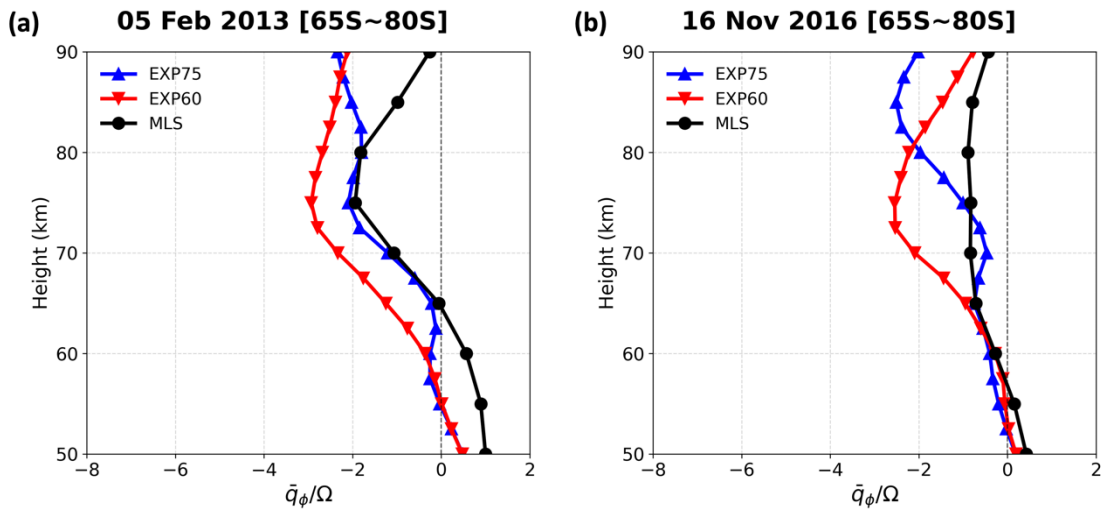
572

573   **Figure 6.** $\bar{q}_\phi$ (normalized by Ω) averaged over 65°S–85°S for (a) 5 February 2013 and

574   (b) 16 November 2016 from the EXP75 (blue), EXP60 (red), and MLS (black).

575   The negative $\bar{q}_\phi$ can be induced by latitudinal and vertical curvatures of zonal-

576   mean zonal wind that correspond to the second and third terms (with negative signs) in

577   the right side of (4), respectively. Figure 7 shows the second (top panels) and third

578 (bottom panels) terms, respectively, for 5 February 2013. The differences shown in

579 Figs. 7c and 7f indicate that the larger negative $\bar{q}_\phi$ is located in the lower altitudes in the

580 EXP60 than in EXP75, inducing the larger instability at 65–75 km in height around

581 70°S–80°S in the EXP60, which is consistent with Fig. 6. Note that the positive

582 differences seen at about 65–75 km in the high-latitude regions in Figs. 7c and 7f mean

583 the larger negative $\bar{q}_\phi$ in the EXP60. Also, it is clear that both vertical and horizontal

584 shear contribute the stronger barotropic/baroclinic instability in the EXP60 in the mid-

585 to-upper mesosphere, as shown in Figs. 7a-b and 7d-e. This analysis demonstrates the

586 mesospheric dynamics specified by the MERRA-2 data up to the altitude of 75 km

587 reduces the large-scale instability in the mid-to-upper mesosphere in the EXP75. This is

588 consistent with Sassi et al. (2021) proposed the absence of specification of middle

589 atmosphere dynamics induce the instability in summer mesospheric westward jet,

590 leading large traveling PWs.

591   The wind structure in the MLT region is mainly driven by momentum

592 deposition from PWs and GWs. Harvey et al. (2019) reported that GWs can change

593 significantly the vertical shears, leading enhanced instability and larger traveling PWs in

594 the mesospheric region based on the satellite observations and SD-WACCM

595 simulations. GW forcing is one of the main factors to maintain the necessary conditions

596 of barotropic/baroclinic instability in the modeled mesosphere (Sato et al., 2018).

597 Therefore, in order to better understand the mechanisms underlying the discrepancies in

598 zonal wind fields and the resulting instability in the model, it is important to examine

599 the contribution of resolved wave forcing (EPFD) and GWD forcing on the zonal wind

600 structure in the mesosphere.

05 February 2013 [$\bar{q}_\phi/\Omega$ 2nd term]

05 February 2013 [$\bar{q}_\phi/\Omega$ 3rd term]

601
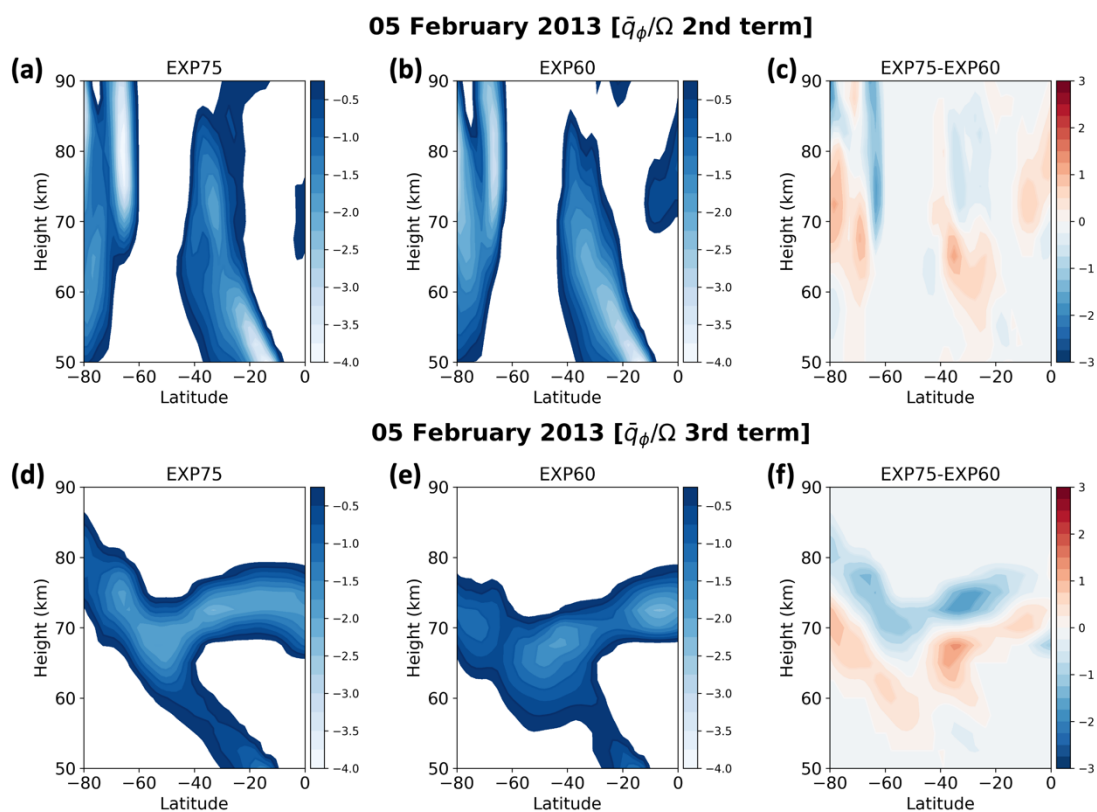
Figure 7. Contributions of (top) the meridional variation of the zonally-averaged mean

flow and (bottom) its vertical variation to the instability condition (negative $\bar{q}_\phi$) shown

in (2), respectively, for 5 February 2013. Panels in each column present the results from

(a and d) the EXP75, (b and e) the EXP60, and (c and f) difference between EXP75 and

EXP60, respectively. Only negative values are plotted except for two panels for

difference.

608   Figure 8 shows the latitude-height distributions of zonal-mean zonal wind, zonal

609   component of GWD and resolved wave forcing (EPFD) in 5 February 2013 for the

610   EXP75, the EXP60, and the difference between EXP75 and EXP60 (EXP75–EXP60).

611   The zonal-mean zonal wind, zonal component of GWD, and resolved wave forcing

612   (EPFD) are calculated through the 21-day averaging (central date ± 10 days). For GWD,

613   the orographic and nonorographic values are added. In Figs. 8a–b, zero-wind lines are

614   located around 80 km height in the SH mid-latitude region, indicating the reversal of the

615   zonal-mean zonal wind due to the eastward momentum forcing from the GWs and

616   resolved waves. It is clear that the zero-wind line in the EXP60 is located at lower

617   altitudes by about 5 km compared to the EXP75, which means that eastward GWD and

618   eastward EPFD from the EXP60 can be larger below the altitude of ~80 km than that

619   from EXP75. Indeed, the difference field between EXP75 and EXP60 for GWD (Fig.

620   8f) shows that the eastward GWD from the EXP60 is larger around (60°S, 70 km) than

621   that from EXP75 as indicated by the negative difference field in those regions. In

622   addition, the resolved wave forcing (EP flux divergence) is more eastward above the

623   altitude of 70 km in the mid-to-high latitude regions in the EXP60 than in the EXP75.

624   This result indicates that the eastward resolved wave forcing also contributes more in

625   the mid-to-upper mesosphere in the EXP60, resulting in the zonal-mean zonal wind

626   reversal (westward to eastward wind) in the lower altitude in the EXP60, as shown

627   around 60°S in Fig. 8b.

628   As mentioned before, the amplification or modulation of westward-propagating

629   PWs with zonal wavenumber 1 and a quasi-10-day period due to NCGWD and resolved

630   GW is negligible (Fig. S3 in Supplement), indicating that the amplification of Q10DW

631   or Q10DO is mainly related to the baroclinic/barotropic instability. The stronger

632   instability in the EXP60 around the altitude of 70 km indicates that WACCM simulates

633   a large meridional and vertical variation of zonal winds compared to the observations in

634   the mid-to-upper mesosphere, which is likely due to the stronger eastward GWD and

635   eastward EPFD forcing near 70 km altitude in the EXP60, as shown in Fig. 8. Cohen et

636   al. (2013) reported that parameterized GWs can generate instability that can generate

637   resolved waves of which forcing (i.e., EPFD) can compensate GWD. Our results show

638   that the increased eastward GWD at 70 km altitude generates instability and it leads

639   more Q10DO. The EPFD in the EXP60 gives the more eastward forcing above 70 km

640   enhancing the wind reversal in the mid-to-high latitudes. However, comparison of Figs.

641   8f and 8i indicates that the structures of GWD and EPFD are roughly 90°–180° shifted

642   in the vertical direction, approximately consistent with the compensation between GWD

643   and EPFD. Raising the nudging altitude of MERRA-2 reanalysis data to 75 km from 60

644   km reduces the instability in the mid-to-upper mesosphere, leading to decreased the

645   Q10DO activity in the EXP75. Therefore, we suggest that strong eastward GWD in the

646   mid-to-upper mesosphere in summer need to be alleviated, which can generate more

647   instability in the SH high-latitude mesosphere region that can lead to discrepancy from

648   observations.
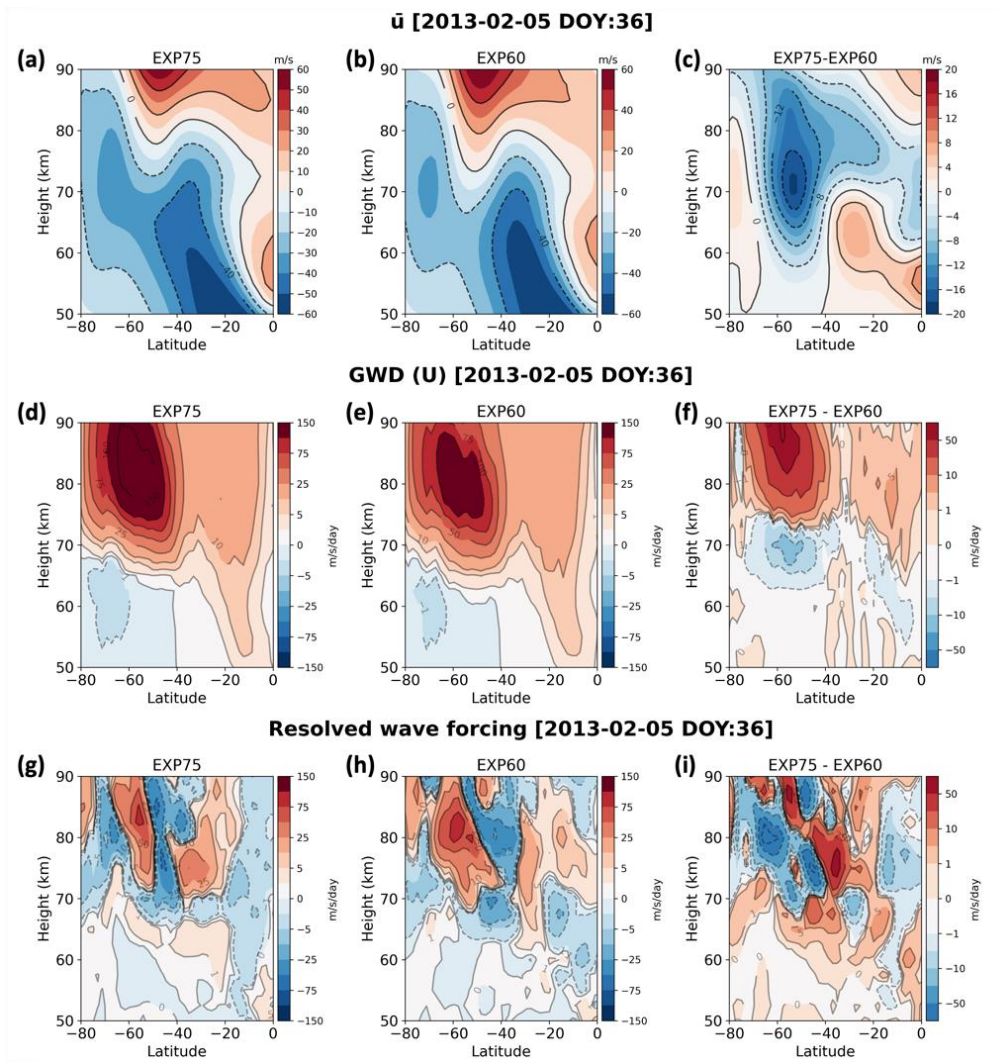
Figure 8. Latitude-height distributions of (a–c) zonal-mean zonal wind, (d–f) zonal

component of GWD and (g–i) resolved wave forcing (EP flux divergence) in 5 February

2013 for (left) the EXP75, (middle) the EXP60, and (right) difference between EXP75

and EXP60 (EXP75–EXP60).

4. ~~Summary~~Conclusions

In this paper, the seasonal variation and the amplification mechanism of Q10DW during 2012–2016 in the SH high-latitude regions are investigated using two MRs located in Antarctica, and SD-WACCM simulations. Using the phase difference of meridional winds measured by two MRs, we extract westward-propagating Q10DW with zonal wavenumber 1. The seasonal variation of the observed Q10DW shows that the amplitude is strong during equinoxes, which is consistent with previous studies. In addition, our study shows the Q10DWs from the MLS appear to be consistently overestimated compared to those from MRs. These discrepancies can be due to both errors in estimating winds from the MLS and uncertainties in results obtained from two MR stations alone. Further investigation is required for more reliable estimation of the amplitude and phase of Q10DWs from observations.

In order to elucidate the amplification mechanism of Q10DW observed by MRs during equinoxes, two SD-WACCM experiments are carried out using the MERRA-2 reanalysis data from surface to ~60 km (EXP60) and ~75 km (EXP75), respectively. The temporal variation of the averaged amplitude of Q10DW in the EXP75 during 2012–2016 is in better agreement with the MR observations. Meanwhile, the amplitude of Q10DW in the EXP60 is excessively large compared with the observations. Based on the analysis of meridional gradient of the QGPV and wave-activity density, the Q10DW observed in the SH high-latitude region by the MRs originated in situ around the high-latitude stratosphere-mesosphere region, where the large-scale instability or overreflection near the critical lines occur. The unrealistically large magnitude of Q10DO (quasi-10-day-like oscillations without satisfying the hemispheric symmetry

678   unlike Q10DW) is simulated in the EXP60 during February and November. In order to

679   understand mechanisms of the large amplitude of Q10DO in the EXP60 during the SH

680   summer, we compare the meridional gradient of QGPV from EXP75 and EXP60. The

681   results show that specified dynamics with MERRA-2 reanalysis data mitigate the

682   meridional and vertical variation of zonal winds in the polar mid-to-upper mesosphere

683   in the EXP75, resulting in leading reduction in the large-scale instability. On the other

684   hand, the large amplitude of Q10DO in the EXP60 is attributed to the large-scale

685   instability related to the GWD and partially to the EPFD in the polar mid-to-upper

686   mesosphere.

687   The polar mesospheric GWD can lead to strong large-scale instability in the SH

688   high-latitude mesosphere and unrealistically large amplitude of Q10DO in summer. The

689   present study on the amplification mechanism of Q10DW during equinoxes, and the

690   unrealistic Q10DO amplitude in summer provide potential importance of large-scale

691   instability, which can be to a substantial degree caused by parameterized GWD, during

692   summer in the polar mesosphere for numerical models. In this paper, we focus on the

693   Q10DW relating to the large-scale instability and polar mesospheric GWD, but other

694   normal modes of PW will be considered for future studies.

695   Results of SD-WACCM may depend on the extra damping above the middle

696   mesosphere in the GEOS-6 model (Fujiwara et al., 2017) used to produce the MERRA-

697   2 data. The damping may have harmful effects on the results for the upper mesosphere

698   in the EXP75, where the dynamics is still specified above the middle mesosphere using

699   the MERRA-2, but comparison with observations shows that the zonal asymmetric

700   structure of mesospheric temperature in the EXP75 is reasonable for the time periods of

our interest (Fig. S5). However, the activity and variability of mesospheric PWs in the MERRA-2 and SD-WACCM need to be further examined for the longer time periods and evaluated against other observations to support the reliability of results obtained in this study, which should be a topic of continuing research.

Code and Data availability

The source code of Community Earth System Model 2 (CESM2) developed at the National Center for Atmospheric Research (NCAR) is available at https://www.cesm.ucar.edu/models/cesm2. The atmospheric forcing data for specified dynamics are available from NCAR Research Data Archive (RDA) at https://rda.ucar.edu.

The Davis station meteor radar data are available from the Australian Antarctic Data Centre at https://data.aad.gov.au/metadata/records/Davis_33MHz_Meteor_Radar. The King Sejong Station meteor radar data are available from Korea Polar Data Center (KPDC) at https://kpdc.kopri.re.kr. The GPH data from the MLS onboard the NASA's EOS Aura satellite are available from Goddard Earth Science Data and Information Services Center (GES DISC) at https://daac.gsfc.nasa.gov.

Author contributions

WL and ISS designed the study, together with YHK, and wrote the manuscript. WL performed the analysis of the observational (MR and satellite) data in collaboration with ISS. ISS designed the SD-WACCM experiments. WL and ISS carried out the SD-

722 WACCM experiments, ISS and BGS aided in interpreting the analysis of action

723 conservation equation for Rossby waves. All authors discussed the results and

724 contributed to the final manuscript.

725 **Competing interests**

726   The authors declare that they have no conflict of interest.

727 **Acknowledgements**

728   This research was supported by the Korea Astronomy and Space Science

729 Institute under the R&D programs (Project No. 2023-1-850-07 and 2024-1-850-02)

730 supervised by the Ministry of Science and ICT. The second author (In-Sun Song) was

731 supported by the Yonsei University Research Funds of 2022 and 2023 (2022-22-0098

732 and 2023-22-0095).

733

734 **References**

735 Andrews, D. G., Holton, J. R., and Leovy, C. B.: Middle Atmosphere Dynamics,

736 Elsevier, New York, USA, 489 pp., 1987.

737 Beres, J. H., Garcia, R. R., Boville, B. A., and Sassi, F.: Implementation of a gravity

738 wave source spectrum parameterization dependent on the properties of convection in the

739 Whole Atmosphere Community Climate Model (WACCM), J. Geophys. Res.-Atmos.,

740 110, https://doi.org/10.1029/2004jd005504, 2005.

741 Brakebusch, M., Randall, C. E., Kinnison, D. E., Tilmes, S., Santee, M. L., and

742 Manney, G. L.: Evaluation of Whole Atmosphere Community Climate Model

743 simulations of ozone during Arctic winter 2004–2005, J. Geophys. Res.-Atmos., 118,

744 2673–2688, https://doi.org/10.1002/jgrd.50226, 2013.

745 Chandran, A., Garcia, R. R., Collins, R. L., and Chang, L. C.: Secondary planetary

746 waves in the middle and upper atmosphere following the stratospheric sudden warming

747 event of January 2012, Geophys. Res. Lett., 40, 1861–1867,

748 https://doi.org/10.1002/grl.50373, 2013.

749 Charron, M. and Manzini, E.: Gravity waves from fronts: Parameterization and middle

750 atmosphere response in a general circulation model, J. Atmos. Sci., 59, 923–941,

751 https://doi.org/10.1175/1520-0469(2002)059<;0923:gwffpa>2.0.co;2, 2002.

752 Cohen, N. Y., Gerber, E. P. and Bühler, O.: Compensation between resolved and

753 unresolved wave driving in the stratosphere: Implications for downward control, J.

754 Atmos. Sci., 70, 3780–3798, https://doi.org/10.1175/jas-d-12-0346.1, 2013.

755 Danabasoglu, G., Lamarque, J. -F., Bacmeister, J., Bailey, D. A., DuVivier, A. K.,

756 Edwards, J., Emmons, L. K., Fasullo, J., Garcia, R., Gettelman, A., Hannay, C.,

757 Holland, M. M., Large, W. G., Lauritzen, P. H., Lawrence, D. M., Lenaerts, J. T. M.,

758 Lindsay, K., Lipscomb, W. H., Mills, M. J., Neale, R., Oleson, K. W., Otto-Bliesner, B.,

759 Phillips, A. S., Sacks, W., Tilmes, S., Kampenhout, L., Vertenstein, M., Bertini, A.,

760 Dennis, J., Deser, C., Fischer, C., Fox-Kemper, B., Kay, J. E., Kinnison, D., Kushner, P.

761 J., Larson, V. E., Long, M. C., Mickelson, S., Moore, J. K., Nienhouse, E., Polvani, L.,

762 Rasch, P. J., and Strand, W. G.: The Community Earth System Model Version 2

763 (CESM2), J. Adv. Model. Earth. Sy., 12, https://doi.org/10.1029/2019ms001916, 2020.

764 Day, K. A. and Mitchell, N. J.: The 5-day wave in the Arctic and Antarctic mesosphere

765 and lower thermosphere, J. Geophys. Res.-Atmos., 1984–2012, 115,

766 https://doi.org/10.1029/2009jd012545, 2010.

767 Edmon, H. J., Hoskins, B. J., and McIntyre, M. E.: Eliassen-Palm cross sections for the

768 troposphere, J. Atmos. Sci., 37, 2600–2616, https://doi.org/10.1175/1520-

769 0469(1980)037<;2600:epcsft>2.0.co;2, 1980.

770 Egito, F., Takahashi, H., and Miyoshi, Y.: Effects of the planetary waves on the MLT

771 airglow, Ann. Geophys., 35, 1023–1032, https://doi.org/10.5194/angeo-35-1023-2017,

772 2017.

773 Eswaraiah, S., Kim, Y. H., Hong, J., Kim, J.-H., Ratnam, M. V., Chandran, A., Rao, S.

774 V. B., and Riggin, D.: Mesospheric signatures observed during 2010 minor

775 stratospheric warming at King Sejong Station (62°S, 59°W), J. Atmos. Sol-Terr. Phy.,

776 140, 55–64, https://doi.org/10.1016/j.jastp.2016.02.007, 2016.

777 Eswaraiah, S., Ratnam, M. V., Kim, Y. H., Kumar, K. N., Chalapathi, G. V.,

778 Ramanajaneyulu, L., Lee, J., Prasanth, P. V., Thyagarajan, K., and Rao, S. V. B.:

779 Advanced meteor radar observations of mesospheric dynamics during 2017 minor SSW

780 over the tropical region, Adv. Space. Res., 64, 1940–1947,

781 https://doi.org/10.1016/j.asr.2019.05.039, 2019.

782 Eyring, Veronika, et al.: Overview of IGAC/SPARC Chemistry-Climate Model

783 Initiative (CCMI) community simulations in support of upcoming ozone and climate

784 assessments, SPARC newsletter, 40, 48–66, https://oceanrep.geomar.de/id/eprint/20227,

785 2013.

786 Forbes, J. M. and Zhang, X.: Quasi-10-day wave in the atmosphere, J. Geophys. Res.-

787 Atmos., 120, 11,079–11,089, https://doi.org/10.1002/2015jd023327, 2015.

788 Forbes, J. M. and Zhang, X.: The quasi-6 day wave and its interactions with solar tides,

789 J. Geophys. Res.-Space, 122, 4764–4776, https://doi.org/10.1002/2017ja023954, 2017.

790 Forbes, J. M., Hagan, M. E., Miyahara, S., Vial, F., Manson, A. H., Meek, C. E., and

791 Portnyagin, Y. I.: Quasi 16-day oscillation in the mesosphere and lower thermosphere,

792 J. Geophys. Res.-Atmos., 100, 9149–9163, https://doi.org/10.1029/94jd02157, 1995.

793 Forbes, J. M., Zhang, X., Heelis, R., Stoneback, R., Englert, C. R., Harlander, J. M.,

794 Harding, B. J., Marr, K. D., Makela, J. J., and Immel, T. J.: Atmosphere-Ionosphere (A-

795 I) coupling as viewed by ICON: Day-to-day variability due to planetary wave (PW)-tide

796 interactions, J. Geophys. Res.-Space, 126, https://doi.org/10.1029/2020ja028927, 2021.

797 Fujiwara, M., Wright, J. S., Manney, G. L., Gray, L. J., Anstey, J., Birner, T., Davis, S.,

798 Gerber, E. P., Harvey, V. L., Hegglin, M. I., Homeyer, C. R., Knox, J. A., Krüger, K.,

799 Lambert, A., Long, C. S., Martineau, P., Molod, A., Monge-Sanz, B. M., Santee, M. L.,

800 Tegtmeier, S., Chabrillat, S., Tan, D. G. H., Jackson, D. R., Polavarapu, S., Compo, G.

801 P., Dragani, R., Ebisuzaki, W., Harada, Y., Kobayashi, C., McCarty, W., Onogi, K.,

802 Pawson, S., Simmons, A., Wargan, K., Whitaker, J. S., and Zou, C.-Z.: Introduction to

803   the SPARC Reanalysis Intercomparison Project (S-RIP) and overview of the reanalysis

804   systems, Atmos. Chem. Phys., 17, 1417–1452, https://doi.org/10.5194/acp-17-1417-

805   2017, 2017.

806   Gan, Q., Oberheide, J., and Pedatella, N. M.: Sources, sinks, and propagation

807   characteristics of the quasi 6-day wave and its impact on the residual mean circulation,

808   J. Geophys. Res.-Atmos., 123, 9152–9170, https://doi.org/10.1029/2018jd028553, 2018.

809   Gelaro, R., McCarty, W., Suárez, M. J., Todling, R., Molod, A., Takacs, L., Randles, C.

810   A., Darmenov, A., Bosilovich, M. G., Reichle, R., Wargan, K., Coy, L., Cullather, R.,

811   Draper, C., Akella, S., Buchard, V., Conaty, A., Silva, A. M. da, Gu, W., Kim, G.-K.,

812   Koster, R., Lucchesi, R., Merkova, D., Nielsen, J. E., Partyka, G., Pawson, S., Putman,

813   W., Rienecker, M., Schubert, S. D., Sienkiewicz, M., and Zhao, B.: The Modern-Era

814   Retrospective Analysis for Research and Applications, Version 2 (MERRA-2), J.

815   Climate, 30, 5419–5454, https://doi.org/10.1175/jcli-d-16-0758.1, 2017.

816   Goncharenko, L. P., Harvey, V. L., Greer, K. R., Zhang, S. -R., and Coster, A. J.:

817   Longitudinally dependent low-latitude ionospheric disturbances linked to the Antarctic

818   sudden stratospheric warming of September 2019, J. Geophys. Res.-Space, 125,

819   https://doi.org/10.1029/2020ja028199, 2020.

820   Harvey, V. L., Knox, J. A., France, J. A., Fujiwara, M., Gray, L., Hirooka, T.,

821   Hitchcock, P., Hitchman, M., Kawatani, Y., Manney, G. L., McCormack, J., Orsolini,

822   Y., Sakazaki, T., and Tomikawa, Y.: Chapter 11: Upper Stratosphere and Lower

823   Mesosphere, SPARC Reanalysis Intercomparison Project (S-RIP) Final Report, edited

824   by: Fujiwara, M., Manney, G. L., Gray, L. J., and Wright, J. S., SPARC Report No. 10,

825 WCRP-6/2021, SPARC, DLR-IPA, Oberpfaffenhofen, Germany,

826 https://doi.org/10.17874/800dee57d13, 2021.

827 Harvey, V. L., Randall, C. E., Becker, E., Smith, A. K., Bardeen, C. G., France, J. A.,

828 and Goncharenko, L. P.: Evaluation of the mesospheric polar vortices in WACCM, J.

829 Geophys. Res.-Atmos., 124, 10626–10645, https://doi.org/10.1029/2019jd030727,

830 2019.

831 He, M., Chau, J. L., Stober, G., Li, G., Ning, B., and Hoffmann, P.: Relations between

832 semidiurnal tidal variants through diagnosing the zonal wavenumber using a phase

833 differencing technique based on two ground-based detectors, J. Geophys. Res.-Atmos.,

834 123, 4015–4026, https://doi.org/10.1002/2018jd028400, 2018.

835 He, M., Chau, J. L., Forbes, J. M., Thorsen, D., Li, G., Siddiqui, T. A., Yamazaki, Y.,

836 and Hocking, W. K.: Quasi-10-day wave and semidiurnal tide nonlinear interactions

837 during the Southern Hemispheric SSW 2019 observed in the Northern Hemispheric

838 mesosphere, Geophys. Res. Lett., 47, https://doi.org/10.1029/2020gl091453, 2020a.

839 He, M., Yamazaki, Y., Hoffmann, P., Hall, C. M., Tsutsumi, M., Li, G., and Chau, J. L.:

840 Zonal wave number diagnosis of Rossby wave-like oscillations using paired ground-

841 based radars, J. Geophys. Res.-Atmos., 125, https://doi.org/10.1029/2019jd031599,

842 2020b.

843 Hirooka, T.: Normal mode Rossby waves as revealed by UARS/ISAMS observations, J.

844 Atmos. Sci., 57, 1277–1285, https://doi.org/10.1175/1520-

845 0469(2000)057<1277:NMRWAR>2.0.CO;2, 2000.

846   Holdsworth, D. A., Murphy, D. J., Reid, I. M., and Morris, R. J.: Antarctic meteor

847   observations using the Davis MST and meteor radars, Adv. Space Res., 42, 143–154,

848   https://doi.org/10.1016/j.asr.2007.02.037, 2008.

849   Huang, C., Zhang, S., Chen, G., Zhang, S., and Huang, K.: Planetary wave

850   characteristics in the lower atmosphere over Xianghe (117.00°E, 39.77°N), China,

851   revealed by the Beijing MST radar and MERRA data, J. Geophys. Res.-Atmos., 122,

852   9745–9758, https://doi.org/10.1002/2017jd027029, 2017.

853   Huang, C., Li, W., Zhang, S., Chen, G., Huang, K., and Gong, Y.: Investigation of

854   dominant traveling 10-day wave components using long-term MERRA-2 database,

855   Earth Planets Space, 73, 85, https://doi.org/10.1186/s40623-021-01410-7, 2021.

856   Huang, Y.-Y., Cui, J., Li, H.-J., and Li, C.-Y.: Inter-annual variations of 6.5-day

857   planetary waves and their relations with QBO, Earth Planet. Phys., 6, 135–148,

858   https://doi.org/10.26464/epp2022005, 2022.

859   Jablonowski, C. and Williamson, D. L.: Numerical techniques for global atmospheric

860   models, Lect. Notes Comput. Sci. Eng., 381–493, https://doi.org/10.1007/978-3-642-

861   11640-7_13, 2011.

862   Lee, W., Song, I., Kim, J., Kim, Y. H., Jeong, S., Eswaraiah, S., and Murphy, D. J.: The

863   observation and SD-WACCM simulation of planetary wave activity in the middle

864   atmosphere during the 2019 Southern Hemispheric sudden stratospheric warming, J.

865   Geophys. Res.-Space, 126, https://doi.org/10.1029/2020ja029094, 2021.

866 Lee, W., Lee, C., Kim, J., Kam, H., and Kim, Y. H.: A modeling analysis of the

867 apparent linear relation between mesospheric temperatures and meteor height

868 distributions measured by a meteor radar, J. Geophys. Res.-Space, 127,

869 https://doi.org/10.1029/2021ja029812, 2022.

870 Lee, W., Kim, Y. H., Lee, C., and Wu, Q.: First comparison of mesospheric winds

871 measured with a Fabry-Perot interferometer and meteor radar at the King Sejong Station

872 (62.2°S, 58.8°W), J. Astron. Space Sci., https://doi.org/10.5140/JASS.2018.35.4.235,

873 2018

874 Li, W., Huang, C., and Zhang, S.: Global characteristics of the westward-propagating

875 quasi-16-day wave with zonal wavenumber 1 and the connection with the 2012/2013

876 SSW revealed by ERA-Interim, Earth Planets Space, 73, 113,

877 https://doi.org/10.1186/s40623-021-01431-2, 2021.

878 Lindzen, R. S., Farrell, B., and Tung, K.-K.: The concept of wave overreflection and its

879 application to baroclinic instability, J. Atmos. Sci., 37, 44–63,

880 https://doi.org/10.1175/1520-0469(1980)037<;0044:tcowoa>2.0.co;2, 1980.

881 Liu, G., Janches, D., Lieberman, R. S., Moffat-Griffin, T., Mitchell, N. J., Kim, J., and

882 Lee, C.: Wind variations in the mesosphere and lower thermosphere near 60°S latitude

883 during the 2019 Antarctic sudden stratospheric warming, J. Geophys. Res.-Space, 126,

884 https://doi.org/10.1029/2020ja028909, 2021.

885 Liu, G., Janches, D., Ma, J., Lieberman, R. S., Stober, G., Moffat-Griffin, T., Mitchell,

886 N. J., Kim, J., Lee, C., and Murphy, D. J.: Mesosphere and lower thermosphere winds

887 and tidal variations during the 2019 Antarctic sudden stratospheric warming, J.

888 Geophys. Res.-Space, 127, https://doi.org/10.1029/2021ja030177, 2022.

889 Luo, J., Gong, Y., Ma, Z., Zhang, S., Zhou, Q., Huang, C., Huang, K., Yu, Y., and Li,

890 G.: Study of the quasi 10-day waves in the MLT region during the 2018 February SSW

891 by a meteor radar chain, J. Geophys. Res.-Space, 126,

892 https://doi.org/10.1029/2020ja028367, 2021.

893 Ma, Z., Gong, Y., Zhang, S., Xiao, Q., Xue, J., Huang, C., and Huang, K.:

894 Understanding the excitation of quasi-6-day waves in both hemispheres during the

895 September 2019 Antarctic SSW, J. Geophys. Res.-Atmos., 127,

896 https://doi.org/10.1029/2021jd035984, 2022.

897 Marsh, D. R., Mills, M. J., Kinnison, D. E., Lamarque, J.-F., Calvo, N., and Polvani, L.

898 M.: Climate change from 1850 to 2005 simulated in CESM1(WACCM), J. Climate, 26,

899 130509150556003, https://doi.org/10.1175/jcli-d-12-00558.1, 2013.

900 Matsuno, T.: Vertical propagation of stationary planetary waves in the winter Northern

901 Hemisphere, J. Atmos. Sci., 27, 871–883, https://doi.org/10.1175/1520-

902 0469(1970)027<;0871:vpospw>2.0.co;2, 1970.

903 Matthias, V. and Ern, M.: On the origin of the mesospheric quasi-stationary planetary

904 waves in the unusual Arctic winter 2015/2016, Atmos. Chem. Phys., 18, 4803–4815,

905 https://doi.org/10.5194/acp-18-4803-2018, 2018.

906 Matthias, V., Hoffmann, P., Rapp, M., and Baumgarten, G.: Composite analysis of the

907 temporal development of waves in the polar MLT region during stratospheric

908 warmings, J. Atmos. Sol.-Terr. Phys., 90, 86–96,

909 https://doi.org/10.1016/j.jastp.2012.04.004, 2012.

910 McCormack, J. P., Harvey, V. L., Randall, C. E., Pedatella, N., Koshin, D., Sato, K.,

911 Coy, L., Watanabe, S., Sassi, F., and Holt, L. A.: Intercomparison of middle

912 atmospheric meteorological analyses for the Northern Hemisphere winter 2009–2010,

913 Atmos. Chem. Phys., 21, 17577–17605, https://doi.org/10.5194/acp-21-17577-2021,

914 2021.

915 McFarlane, N. A.: The effect of orographically excited gravity wave drag on the general

916 circulation of the lower stratosphere and troposphere, J. Atmos. Sci., 44, 1775–1800,

917 https://doi.org/10.1175/1520-0469(1987)044<;1775:teooeg>2.0.co;2, 1987.

918 Meyer, C. K. and Forbes, J. M.: A 6.5-day westward propagating planetary wave:

919 Origin and characteristics, J. Geophys. Res.-Atmos., 102, 26173–26178,

920 https://doi.org/10.1029/97jd01464, 1997.

921 Mitra, G., Guharay, A., Batista, P. P., and Buriti, R. A.: Impact of the September 2019

922 minor sudden stratospheric warming on the low-latitude middle atmospheric planetary

923 wave dynamics, J. Geophys. Res.-Atmos., 127, https://doi.org/10.1029/2021jd035538,

924 2022.

925 Palmer, T. N.: Properties of the Eliassen-Palm flux for planetary scale motions, J.

926 Atmos. Sci., 39, 992–997, https://doi.org/10.1175/1520-

927 0469(1982)039<;0992:potepf>2.0.co, 1982.

928 Qin, Y., Gu, S., Dou, X., Gong, Y., Chen, G., Zhang, S., and Wu, Q.: Climatology of

929 the quasi-6-day wave in the mesopause region and its modulations on total electron

930 content during 2003–2017, J. Geophys. Res.-Space, 124, 573–583,

931 https://doi.org/10.1029/2018ja025981, 2019.

932 Qin, Y., Gu, S., Dou, X., Teng, C., Yang, Z., and Sun, R.: Southern Hemisphere

933 response to the secondary planetary waves generated during the Arctic sudden

934 stratospheric final warmings: Influence of the quasi-biennial oscillation, J. Geophys.

935 Res.-Atmos., 127, https://doi.org/10.1029/2022jd037730, 2022.

936 Qin, Y., Gu, S., Teng, C., Dou, X., Yu, Y., and Li, N.: Comprehensive study of the

937 climatology of the quasi-6-day wave in the MLT region based on Aura/MLS

938 observations and SD-WACCM-X simulations, J. Geophys. Res.-Space, 126,

939 https://doi.org/10.1029/2020ja028454, 2021.

940 Reynolds, R. W., Rayner, N. A., Smith, T. M., Stokes, D. C., and Wang, W.: An

941 improved in situ and satellite SST analysis for climate, J. Climate, 15, 1609–1625,

942 https://doi.org/10.1175/1520-0442(2002)015<;1609:aiisas>2.0.co;2, 2002.

943 Rhodes, C. T., Limpasuvan, V., and Orsolini, Y. J.: Eastward-propagating planetary

944 waves prior to the January 2009 sudden stratospheric warming, J. Geophys. Res.-

945 Atmos., 126, https://doi.org/10.1029/2020jd033696, 2021.

946 Richter, J. H., Sassi, F., and Garcia, R. R.: Toward a physically based gravity wave

947 source parameterization in a general circulation model, J. Atmos. Sci., 67, 136–156,

948 https://doi.org/10.1175/2009jas3112.1, 2010.

949   Salby, M. L.: Rossby normal modes in nonuniform background configurations. Part I:

950   Simple fields, J. Atmos. Sci., 38, 1803–1826, https://doi.org/10.1175/1520-

951   0469(1981)038<;1803:rnminb>2.0.co;2, 1981a.

952   Salby, M. L.: Rossby normal modes in nonuniform background configurations. Part II.

953   Equinox and solstice conditions, J. Atmos. Sci., 38, 1827–1840,

954   https://doi.org/10.1175/1520-0469(1981)038<;1827:rnminb>2.0.co;2, 1981b.

955   Salby, M. L.: Survey of planetary-scale traveling waves: The state of theory and

956   observations, Rev. Geophys., 22, 209–236, https://doi.org/10.1029/rg022i002p00209,

957   1984.

958   Sassi, F., McCormack, J. P., Tate, J. L., Kuhl, D. D., and Baker, N. L.: Assessing the

959   impact of middle atmosphere observations on day-to-day variability in lower

960   thermospheric winds using WACCM-X, J. Atmos. Sol.-Terr. Phys., 212, 105486,

961   https://doi.org/10.1016/j.jastp.2020.105486, 2021.

962   Sassi, F. and Liu, H.-L.: Westward traveling planetary wave events in the lower

963   thermosphere during solar minimum conditions simulated by SD-WACCM-X, J.

964   Atmos. Sol.-Terr. Phys., 119, 11–26, https://doi.org/10.1016/j.jastp.2014.06.009, 2014.

965   Sato, K., Yasui, R., and Miyoshi, Y.: The momentum budget in the stratosphere,

966   mesosphere, and lower thermosphere. Part I: Contributions of different wave types and

967   in situ generation of Rossby waves, J. Atmos. Sci., 75, 3613–3633,

968   https://doi.org/10.1175/jas-d-17-0336.1, 2018.

969 Schwartz, M. J., Lambert, A., Manney, G. L., Read, W. G., Livesey, N. J., Froidevaux,

970 L., Ao, C. O., Bernath, P. F., Boone, C. D., Cofield, R. E., Daffer, W. H., Drouin, B. J.,

971 Fetzer, E. J., Fuller, R. A., Jarnot, R. F., Jiang, J. H., Jiang, Y. B., Knosp, B. W.,

972 Krüger, K., Li, J. -L. F., Mlynczak, M. G., Pawson, S., Russell, J. M., Santee, M. L.,

973 Snyder, W. V., Stek, P. C., Thurstans, R. P., Tompkins, A. M., Wagner, P. A., Walker,

974 K. A., Waters, J. W., and Wu, D. L.: Validation of the Aura Microwave Limb Sounder

975 temperature and geopotential height measurements, J. Geophys. Res.-Atmos. 1984

976 2012, 113, https://doi.org/10.1029/2007jd008783, 2008.

977 Song, B.-G., Chun, H.-Y., and Song, I.-S.: Role of gravity waves in a vortex-split

978 sudden stratospheric warming in January 2009, J. Atmos. Sci., 77, 3321–3342,

979 https://doi.org/10.1175/jas-d-20-0039.1, 2020.

980 Thorncroft, C. D., Hoskins, B. J., and McIntyre, M. E.: Two paradigms of baroclinic-

981 wave life-cycle behaviour, Q. J. Roy. Meteor. Soc., 119, 17–55,

982 https://doi.org/10.1002/qj.49711950903, 1993.

983 Torrence, C. and Compo, G. P.: A practical guide to wavelet analysis, B. Am. Meteorol.

984 Soc., 79, 61–78, https://doi.org/10.1175/1520-0477(1998)079<0061:apgtwa>2.0.co;2,

985 1998.

986 Walker, S. N., Sahraoui, F., Balikhin, M. A., Belmont, G., Pinçon, J. L., Rezeau, L.,

987 Alleyne, H., Cornilleau-Wehrlin, N., and André, M.: A comparison of wave mode

988 identification techniques, Ann. Geophys., 22, 3021–3032,

989 https://doi.org/10.5194/angeo-22-3021-2004, 2004.

990   Wang, J. C., Palo, S. E., Forbes, J. M., Marino, J., Moffat-Griffin, T., and Mitchell, N.

991   J.: Unusual Quasi 10-Day Planetary wave activity and the ionospheric response during

992   the 2019 Southern Hemisphere sudden Stratospheric Warming, J. Geophys. Res.-Space,

993   126, https://doi.org/10.1029/2021ja029286, 2021.

994   Yamazaki, Y. and Matthias, V.: Large-amplitude quasi-10-day waves in the middle

995   atmosphere during final warmings, J. Geophys. Res.-Atmos., 124, 9874–9892,

996   https://doi.org/10.1029/2019jd030634, 2019.

997   Yin, S., Ma, Z., Gong, Y., Zhang, S., and Li, G.: Response of quasi-10-day waves in the

998   MLT region to the sudden stratospheric warming in March 2020, Adv. Space Res., 71,

999   298–305, https://doi.org/10.1016/j.asr.2022.10.054, 2023.